Lajos Szalmas, Thomas Veltzke, Jorg Thöming

Analysis of the diodic effect of flows of rarefied gases in tapered rectangular channels

Take down policy
If you believe that this document or any material on this site infringes copyright, please contact publizieren@suub.uni-bremen.de with full details and we will remove access to the material.

Analysis of the diodic effect of flows of rarefied gases in tapered rectangular channels

Lajos Szalmás[*], Thomas Veltzke, Jorg Thöming

Center for Environmental Research and Sustainable Technology (UFT), University of Bremen, Leobener Strasse, 28359 Bremen, Germany

ARTICLE INFO

ABSTRACT

Pressure driven flows of rarefied single gases through long tapered rectangular channels are studied computationally. A part of the results is compared to the available experimental data. The flow is modeled by the linearized Bhatnagar-Gross-Krook kinetic equation. The mass flow rate and the distributions of the pressure and the rarefaction parameter are deduced. Calculations are performed in the whole range of the gaseous rarefaction. The diodicity has a maximum at intermediate values of the Knudsen number and increases with large to small cross section ratio. The diodic effect is explained phenomenologically. The pressure profile depends on the flow direction and varies strongly near the small height. The mass flow rates of CO_2, N_2 and Ar gases in a mini/microchannel at moderate rarefactions are compared to the numerical results. An end-correction to the numerical calculation is applied. A relatively good agreement is found between the computational and experimental flow rates. The agreement is improved if the end-correction is used. The experimental diodicity is reproduced well with the numerical simulation. The results presented in the paper might be useful for the development and optimal design of pumping systems based on the diode effect.

1. Introduction

Over the last few years, rarefied gaseous flows through various long channels have received considerable attention. These flows can be relevant in microfludic applications [1] or conventional vacuum science [2]. When the gas flows in a channel of which diameter is comparable with the molecular mean-free-path, the details of the molecular motion can not be neglected. In such cases, the proper description of the gas requires the consideration of the velocity distribution function and kinetic equations.

Significant theoretical and numerical work has been devoted to study pressure driven flows of rarefied gases in various long channels with constant cross sections. When the channel is long, the kinetic problem can be reduced to a two-dimensional one on the cross section sheet. Linearized kinetic models have been solved for single gas flows through capillaries with rectangular [3], circular [4,5], elliptical [6], triangular [7,8], trapezoidal [9] and double trapezoidal [10] cross sections. The McCormack kinetic model for binary gases has also been solved for various channels [11–14]. In the aforementioned works, the kinetic equation is solved by the discrete velocity method, which provides very accurate results numerically with modest computational effort. Within this framework, flows through channels with varying cross sections have also been calculated [15,16].

The experimental work has mainly been based on the measurement of the flow rates of single gases through long microchannels [17–23]. The flow rates have been compared with analytical formulas in the slip flow region and/or kinetic results. A part of these works has also focused on determining the viscous slip coefficients [18] or developing slip flow models [20]. Generally, the majority of previous studies have referred to channels with constant cross sections. Recently, however, some results have been published for tapered rectangular [23,24] and trapeziodal channels [25,26]. In these works, the numerical and experimental investigation refers to the slip flow region. The scope of the present paper is to improve the numerical work of Ref. [24] and extend it to a wide range of the gaseous rarefaction and other flow parameters while keeping the existing experimental data for the comparison.

Channels with monotonically varying cross sections can be useful to develop pumping systems by using their diode effect [27,28]. In such channels, the gaseous flow rate depends on the orientation of the capillary. If the gas flows along the direction of

increasing cross section, the flow rate is larger than in the opposite situation. Previously, this effect has been studied in the slip flow region only. However, it is quite useful to extend the theoretical analysis for the whole range of the gaseous rarefaction.

In this paper, isothermal pressure driven rarefied gaseous flows through long tapered rectangular channels are analyzed computationally at the kinetic level. Some results are compared to the experimental data of Ref. [24]. The cross section of the channel is varying: one dimension, the width of the channel, is fixed, but the height is linearly changing along the axis. The flow problem is locally described by the Bhatnagar-Gross-Krook (BGK) linearized kinetic model, which is solved by an accelerated discrete velocity method. The mass conservation is solved along the axis of the channel in order to deduce the mass flow rate and the distribution of the pressure and the rarefaction parameter. Test calculations are performed in the whole range of the gaseous rarefaction. Particular attention is paid for the diodicity defined as the ratio of the flow rates in the nozzle and diffusor directions. The effects of the rarefaction, pressure ratio and the dimensions of the channel on the flow are analyzed and commented on. The diodic effect is phenomenologically explained. Representative distributions of the rarefaction parameter and the pressure are also shown. The experimental mass flow rate of CO_2, N_2 and Ar gases through a mini/microchannel [24] are compared to the corresponding numerical results at moderate rarefactions. For some parts of the numerical simulation, an end-correction is applied to better describe the end-effect in the experiment.

The main novelty of the paper compared to Ref. [24] consists of 1) the diode phenomenon is analyzed in a wide range of the gas rarefaction from the near continuum to the free molecular domains, 2) the effect of the accommodation coefficient is studied on the flow rates and the diodicity, 3) an explanation is provided for the difference of the flow rates in the nozzle direction and the diffusor one in order to have a better understanding of the phenomenon and 4) the end-effect on the flow rates is analyzed.

2. Model and simulation method

2.1. Statement of the problem

Isothermal pressure driven single gas flows in long tapered microchannels are considered. A particular channel has a rectangular cross section with height H and width W. The length of the channel is denoted by L. The channel axis lies in the Cartesian coordinate direction z', while the cross section is located in the (x', y') coordinate sheet. The width of the channel is constant, but its height is linearly varying along the axis as $H(z') = H_1 + z'(H_2 - H_1)/L$, where H_1 and H_2 are the inlet and outlet heights of the flow configuration, respectively. The length of the channel is considered sufficiently larger than H or W; hence, the gas flows only in the axial direction, and the inlet and outlet effects can be neglected.

The flow is driven by the pressure difference between the inlet and the outlet of the channel. The upstream and downstream pressures are denoted by P_1 and P_2. It is assumed that $P_1 > P_2$; hence, the gas always flows from the inlet to the outlet. Two types of flow configuration depending on the orientation of the channel are investigated. For a given channel, the smallest and largest heights at the two ends of the channel are denoted by H_s and H_l. If $H_1 > H_2$, (i.e. $H_1 = H_l$ and $H_2 = H_s$), the flow direction is referred as *nozzle*, while in the opposite situation, $H_2 > H_1$, (i.e. $H_1 = H_s$ and $H_2 = H_l$), the direction is called *diffusor*.

The gas is characterized by the local rarefaction parameter defined by

$$\delta(z') = \frac{P(z')L_c(z')}{\mu v_0}, \tag{1}$$

where $P(z')$ is the gaseous pressure, μ is the viscosity and $v_0 = \sqrt{2R_g T/m}$ is the most probable molecular speed of the gas. Here, $R_g = 8.314$ J/(mol K) is the universal gas constant, T is the temperature and m is the molar mass of the gas. In the definition of the rarefaction parameter, $L_c(z') = H(z')$ if $H(z') \leq W$, otherwise $L_c(z') = W$. The hydraulic diameter might also be utilized for the definition of the rarefaction parameter; however, using the height or the width is more straightforward since the calculation is simpler in this way. To describe the rarefaction degree of the gas, it is convenient to introduce the Knudsen number $Kn(z') = \sqrt{\pi}/(2\delta)$. For later purposes, the mean Knudsen number for the whole flow configuration is introduced and defined as

$$Kn_m^{(i)} = \frac{1}{L} \int Kn(z')^{(i)} dz', \tag{2}$$

where $i = n, d$ denotes the nozzle or diffusor direction.

The main interest of this work is to calculate the mass flow rate

$$\dot{M} = \frac{2P(z')}{v_0^2} \int_A u'(z') dA, \tag{3}$$

where $u'(z')$ is the axial velocity of the gas and A denotes the cross section of the channel. In order to describe the ratio of the flow rates in the nozzle and diffusor directions, the diodicity is introduced by

$$D = \frac{\dot{M}_n\left(P_{1,d}^2 - P_{2,d}^2\right)}{\dot{M}_d\left(P_{1,n}^2 - P_{2,n}^2\right)}, \tag{4}$$

where the subscripts n, d stand for the nozzle and diffusor directions for the quantities, respectively. The diodicity is also determined and analyzed in the present work. Furthermore, the distributions of the pressure and the rarefaction parameter in the channel are deduced.

2.2. Kinetic solution

The computational calculation refers to the whole range of the gaseous rarefaction. Such an approach requires the consideration of the velocity distribution function of the molecules and the Boltzmann or other kinetic equation. The smallness of H and W compared to L implies that the flow is low-speed, and, consequently, linearized description can be applied.

In the linearized framework, the local mass flow rate can be written by

$$\dot{M} = -G(\delta, a)\frac{HWL_c}{v_0}\frac{dP}{dz'}, \tag{5}$$

where $G(\delta, a)$ is the dimensionless flow rate through the cross section of the channel at local rarefaction parameter δ and aspect ratio a defined by $a = H(z')/W$ if $H(z') \leq W$ and $a = W/H(z')$ otherwise. It follows from the definition that $a \leq 1$.

It is noted that $\dot{M}$ is constant along the channel due to the conservation of mass. In order to find $\dot{M}$, Eq. (5) needs to be integrated. The integration requires the function $G(\delta, a)$ in the whole range of δ and a. Consequently, the solution of the problem is divided into two stages. First, $G(\delta, a)$ is determined by a suitable kinetic calculation in a wide range of δ and a to create a database.

Second, Eq. (5) is integrated to yield $\dot{M}$ and the distributions of the pressure and the rarefaction parameter.

The local two-dimensional flow problem is modeled by the linearized Bhatnagar-Gross-Krook kinetic equation. This model equation is considered physically accurate for isothermal flows. The velocity distribution function is linearized by $f(c,x,y,z) = f^0(c,z)[1 + X_p h(c,x,y)]$, where $x = x'/L_c$, $y = y'/L_c$, $z = z'/L_c$ are the non-dimensional coordinates, $\boldsymbol{c} = \boldsymbol{v}/v_0$ is the dimensionless molecular velocity with $\boldsymbol{v}$ denoting the dimensional molecular velocity, h is the perturbation function, $f^0(\boldsymbol{c},z) = n(z)\pi^{-3/2}v_0^{-3}\exp(-c^2)$ is the local equilibrium distribution function and $X_p = (\partial P/\partial z)L_c/P$ is the dimensionless local pressure gradient. Here, $n(z)$ denotes the molar density of the gas. The kinetic equation for the perturbation function reads as

$$c_x\frac{\partial h}{\partial x} + c_y\frac{\partial h}{\partial y} = -\delta h + \delta 2c_z u - c_z, \qquad (6)$$

where

$$u(x,y) = \pi^{-3/2}\int h(\boldsymbol{c},x,y)c_z e^{-c^2}\, d\boldsymbol{c} \qquad (7)$$

is the dimensionless axial velocity of the gas. At the channel walls, the applied boundary condition for the incoming molecules is diffuse-specular reflection (Maxwell-type). The accommodation coefficient is denoted by σ. The dimensionless flow rate can be obtained by $G = -2\bar{u}$, which is twice the spatial average of the non-dimensional normalized axial velocity.

In the case of the experimental results, the local Knudsen number can be quite small, which requires the proper solution of the kinetic equation near the hydrodynamic region also. For this reason, Eq. (6) is solved by using a variant of the accelerated discrete velocity method [5,8,12,14]. It is known that this method is superior to the standard kinetic solver at very small Knudsen numbers. In the accelerated method, an additional moment equation is derived and solved parallel with the kinetic equation. The accelerated method for the BGK linearized kinetic equation is well-documented in the literature [5,8,12,14]; hence, its description is omitted here for brevity. In the numerical solution, the molecular velocity and spatial spaces are discretized. The molecular velocity is transformed into polar coordinates. The magnitude of the velocity is discretized by 32-point and 16-point Gauss-Legendre quadratures for $\delta \leq 0.05$ and $\delta > 0.05$, while its angle variable in the $(0, \pi/2)$ interval is discretized by using $N_a = [100, 300]$ number of nodes for $\delta \geq 2$ and $\delta < 2$ respectively. Both x, y spatial coordinates are divided into $N = [301, 151]$ number of nodes for $\delta \geq 10$ and $\delta < 10$ respectively. The dimensionless flow rate, $G(\delta, a)$, is calculated by using the non-accelerated and accelerated methods for $\delta < 2$ and $\delta \geq 2$, respectively, for a wide range of δ and a. The above mentioned parameters in the discretization ensure 0.1% numerical accuracy for $G(\delta, a)$. This has been checked by doubling all these parameters. The doubling of the parameters of the discretization does not change $G(\delta, a)$ more than ± 0.1%. The calculated values of $G(\delta, a)$ form a database; hence, the function $G(\delta, a)$ is supposed to be known.

The mass flow rate and the distribution of the pressure can be obtained by solving Eq. (5). The function of the pressure can be quite steep near the end of the channel with the smaller height. Hence, for good numerical accuracy, Eq. (5) is solved by a two-step Runge-Kutta type method. The coordinate along the axis of the channel is discretized as $z_i' = (i-1)\Delta z'$, where $1 \leq i \leq M$ and $\Delta z' = L/(M-1)$. By using the discrete coordinates, the two-step numerical solver reads as

$$P_i^* = P(z_{i-1}') - \frac{\dot{M}}{G\left(\delta_{i-1}, a_i^*\right)}\frac{v_0}{2WH_i^*L_{ci}^*}\Delta z', \qquad (8)$$

$$P(z_i') = P(z_{i-1}') - \frac{\dot{M}}{G\left(\delta_i^*, a_i^*\right)}\frac{v_0}{WH_i^*L_{ci}^*}\Delta z', \qquad (9)$$

where P_i^* is the intermediate value of the pressure, $\delta_{i-1} = \delta(z_{i-1}')$, $H_i^* = H((z_i' + z_{i-1}')/2)$, $L_{ci}^* = L_c((z_i' + z_{i-1}')/2)$, a_i^* is the aspect ratio of $[H_i^*, W]$ and δ_i^* is the intermediate rarefaction parameter calculated on the basis of P_i^* and L_{ci}^*. The integration is carried out by setting $P(0) = P_1$ and solving Eqs. (8)–(9) for $i > 1$ with a fixed $\dot{M}$. By using a bisection method, the optimal $\dot{M}$ which ensures the outlet boundary condition, $P(L) = P_2$, is determined. The outlet boundary condition for P is fulfilled with the relative error of $1e$-7. All integrations have been performed with the resolution $M = 10000$. The proper values of $G(\delta, a)$ in Eqs. (8)–(9) have been determined by linear extrapolation with respect to δ and a by using the pre-computed database for $G(\delta, a)$. In this database, δ and a are represented by 73 and 70 discrete values, respectively. Doubling these numbers (i.e. 73 and 70) and M does not change the results in terms of $\dot{M}$, $P(z')$ and $\delta(z')$ more than ± 0.2%. By using error propagation, the overall absolute numerical accuracy of $\dot{M}$, $P(z')$ and $\delta(z')$ is estimated as the sum of the absolute errors of determining $G(\delta, a)$ and solving Eqs. (8)–(9), which is $0.1\% + 0.2\% = 0.3\%$. Hence, as estimated, $\dot{M}$, $P(z')$ and $\delta(z')$ are determined with numerical error not larger than ± 0.3%.

In the hydrodynamic and free molecular limits, general statements about the mass flow rate can be made. In the hydrodynamic limit, at very high rarefaction parameters, the hydrodynamic solution with no-slip boundary condition can be applied. In this situation, the dimensionless flow rate can be decomposed as a product of two functions such that

$$G(\delta, a) = G_0(\delta)F(a), \qquad (10)$$

where $G_0(\delta)$ and $F(a)$ depend on one variable only, see Ref. [3]. In the hydrodynamic or free molecular limits, $G_0(\delta) = \delta/6$ or $G_0(\delta)$ is constant, respectively. Substituting the expression of Eq. (10) with the particular form of $G_0(\delta)$ into Eq. (5), the resulting equation becomes separable and can be integrated. The separation of the variables reveals that the mass flow rate is independent of the direction of the flow in both hydrodynamic and free molecular limits. This finding indicates that the diodicity defined by Eq. (4) is unity in these cases.

3. Results

3.1. Numerical analysis

The flow rate is calculated numerically for a test channel with geometrical data $H_l/H_s = 120$, $W/H_s = 500$ in a wide range of flow parameters for both nozzle and diffusor directions with complete accommodation $\sigma = 1$. The rarefaction is quantified by the outlet rarefaction parameter of the nozzle case $\delta_2^{(n)}$. The corresponding nozzle and diffusor cases are calculated with the same inlet and outlet pressures to allow for comparison. The results are presented in dimensionless units. In this way, the length of the channel does not play role in the calculation. The dimensionless flow rate is introduced by $Q = \dot{M}v_0 L/(H_s H_l W(P_1 + P_2))$.

Table 1 shows the dimensionless flow rates at various values of $\delta_2^{(n)}$ with fixed pressure ratio $P_1/P_2 = 8$. The columns of the table

Table 1
Flow rates $Q^{(n)}$, $Q^{(d)}$, Knudsen numbers $Kn_m^{(n)}$, $Kn_m^{(d)}$ and diodicity D at $P_1/P_2 = 8$ versus $\delta_2^{(n)}$.

$\delta_2^{(n)}$	$Q^{(n)}$	$Q^{(d)}$	$Kn_m^{(n)}$	$Kn_m^{(d)}$	D
0.01	1.602	1.540	6.78E-1	2.04E+0	1.040
0.02	1.478	1.384	3.33E-1	1.03E+0	1.067
0.03	1.423	1.311	2.19E-1	6.98E-1	1.086
0.05	1.380	1.244	1.28E-1	4.26E-1	1.109
0.07	1.368	1.217	9.02E-2	3.08E-1	1.124
0.10	1.374	1.205	6.19E-2	2.19E-1	1.140
0.20	1.455	1.251	2.97E-2	1.13E-1	1.163
0.30	1.561	1.337	1.93E-2	7.62E-2	1.168
0.50	1.788	1.533	1.12E-2	4.66E-2	1.166
0.70	2.019	1.746	7.85E-3	3.36E-2	1.157
1	2.367	2.074	5.38E-3	2.38E-2	1.141
2	3.522	3.201	2.61E-3	1.20E-2	1.100
3	4.675	4.344	1.71E-3	8.06E-3	1.076
5	6.980	6.642	1.02E-3	4.86E-3	1.051
7	9.287	8.946	7.21E-4	3.47E-3	1.038

from left to right present $\delta_2^{(n)}$, the flow rate for the nozzle and diffusor directions, i.e. $Q^{(n)}$ and $Q^{(d)}$, the mean Knudsen numbers calculated by Eq. (2) for the nozzle and diffusor directions, i.e. $Kn_m^{(n)}$ and $Kn_m^{(d)}$, and the deduced diodicity D. As it can be seen the flow rates exhibit the Knudsen minimum in both cases, and the flow rate is always larger in the nozzle direction than the diffusor one. The investigated gaseous rarefaction spans a wide range from the hydrodynamic and slip regimes to the transition and near free molecular regions. The mean Knudsen number is in the range of $[7.21 \times 10^{-4} - 6.78 \times 10^{-1}]$ and $[3.47 \times 10^{-3} - 2.04]$ for the nozzle and diffusor directions, respectively. The diodicity is always larger than unity. Starting from the high rarefaction range, the diodicity is increasing until it reaches the maximum value 1.168 at $\delta_2^{(n)} = 0.3$, then it starts to decrease down to the hydrodynamic limit. It is recalled that the diodicity is unity in the hydrodynamic and free molecular limits.

Table 2 presents the flow rates as functions of the pressure ratio at $\delta_2^{(n)} = 0.3$ in a similar scenario as Table 1. As it can be seen the flow rates increase with increasing pressure ratio, which is explained by the larger driving force. Starting from $P_1/P_2 = 3$, D increases with increasing P_1/P_2. It reaches a maximum at $P_1/P_2 = 15$, then starts to decrease with further increase of the pressure ratio. The maximum of the diodicity is 1.197. The outlet nozzle rarefaction parameter is fixed at $\delta_2^{(n)} = 0.3$. If P_1/P_2 is small, then the inlet rarefaction parameter is also small; hence, the overall rarefaction is relatively close to the free molecular limit. Consequently, D is nearly unity. If P_1/P_2 is increased, the overall rarefaction shifts to the intermediate region, where the maximum

diodicity is observed. In the present case, this maximum is obtained at $P_1/P_2 = 15$. If P_1/P_2 is further increased, the overall rarefaction tends to the hydrodynamic domain; hence, D starts to decrease.

In Table 3, the effect of the ratio of the large and small heights, i.e. H_l/H_s, is shown. The flow rates are presented at various values of H_l/H_s at outlet nozzle rarefaction parameter $\delta_2^{(n)} = 0.3$ and pressure ratio $P_1/P_2 = 8$. The dimensionless flow rates in both directions monotonically increase if H_l/H_s is increased. The diodicity also increases if H_l/H_s is increased. This is explained by the fact that if H_l/H_s is increased then the channel more and more deviates from a duct with uniform cross section. It is noted that since the height of the channel is linearly varying, the geometrical parameter which describes the strength of this variation is H_l/H_s for a fixed L. Hence, this parameter determines the diodic character from a geometrical point of view.

In Tables 4 and 5, the effect of the accommodation coefficient σ is shown. In Table 4, the flow rates are shown for both nozzle and diffusor directions in terms of $\delta_2^{(n)}$ at $P_1/P_2 = 8$ and three different values of σ for another test channel with $H_l/H_s = 100$ and $W/H_s = 15$. As it can be seen, the flow rate in the nozzle direction is always larger than in the diffusor one at all three values of the accommodation coefficient $\sigma = [1, 0.8, 0.6]$. Hence, the gas exhibits the diode effect independently of σ. As σ is decreased, the flow rates increase since the surface of the channel becomes more slippery. Table 5 presents the diodicity for the flow rates given in Table 4. Comparing the three data at different accommodation coefficients, it can be concluded that D is the largest at full accommodation at $\delta_2^{(n)} = 0.5$.

In Fig. 1, the diodicity is shown at $P_1/P_2 = 8$, $W/H_s = 500$ and $\sigma = 1$ for various values of the ratio H_l/H_s as a function of the average Knudsen number which is defined by $Kn_{av} = (Kn(0)^{(n)} + Kn(L)^{(n)} + Kn(0)^{(d)} + Kn(L)^{(d)})/4$, where n and d refer to the nozzle or diffusor direction. It is noted that Kn_{av} is introduced to characterize the average Knudsen number including both nozzle and diffusor cases. It has no relation to Kn_m. The nozzle and diffusor calculations are performed with the same inlet and outlet pressures as for the results in the tables. It can be seen that the diodicity has a maximum for all aspect ratios in the transition region. By approaching the hydrodynamic and free molecular limits, the diodicity tends to unity. Its maximum increases with increasing H_l/H_s ratio. Hence, it is shown that the diodic effect is stronger if the channel is more tapered. It can also be seen that the maximum of D shifts to larger Kn_{av} as H_l/H_s is increased. Such a dependence is caused by the definition of Kn_{av}.

The diodic effect can be explained phenomenologically well. In Tables 1–3, it can be seen that the mean Knudsen number is smaller in the nozzle direction than the diffusor one. This occurs because the height at the inlet is larger for the nozzle direction than the diffusor one. Larger inlet height with the existence of larger pressure at the inlet results into a smaller mean Knudsen number for

Table 2
Flow rates $Q^{(n)}$, $Q^{(d)}$, Knudsen numbers $Kn_m^{(n)}$, $Kn_m^{(d)}$ and diodicity D at $\delta_2^{(n)} = 0.3$ versus P_1/P_2.

P_1/P_2	$Q^{(n)}$	$Q^{(d)}$	$Kn_m^{(n)}$	$Kn_m^{(d)}$	D
3	0.868	0.798	4.71E-2	9.56E-2	1.088
5	1.230	1.085	2.98E-2	8.55E-2	1.133
7	1.465	1.264	2.19E-2	7.89E-2	1.159
9	1.648	1.402	1.73E-2	7.39E-2	1.176
11	1.806	1.521	1.42E-2	7.00E-2	1.187
13	1.948	1.632	1.21E-2	6.67E-2	1.193
15	2.080	1.739	1.05E-2	6.38E-2	1.196
20	2.385	1.993	7.88E-3	5.80E-2	1.196
30	2.942	2.486	5.19E-3	4.98E-2	1.183
50	3.984	3.465	3.03E-3	3.96E-2	1.150
80	5.496	4.939	1.83E-3	3.08E-2	1.113

Table 3
Flow rates $Q^{(n)}$, $Q^{(d)}$, Knudsen numbers $Kn_m^{(n)}$, $Kn_m^{(d)}$ and diodicity D at $\delta_2^{(n)} = 0.3$ and $P_1/P_2 = 8$ versus H_l/H_s.

H_l/H_s	$Q^{(n)}$	$Q^{(d)}$	$Kn_m^{(n)}$	$Kn_m^{(d)}$	D
2	1.279	1.228	5.36E-1	6.76E-1	1.041
4	1.356	1.247	3.15E-1	5.06E-1	1.088
8	1.433	1.273	1.81E-1	3.69E-1	1.126
16	1.492	1.297	1.03E-1	2.61E-1	1.150
32	1.529	1.316	5.85E-2	1.78E-1	1.162
64	1.550	1.329	3.28E-2	1.16E-1	1.166
128	1.562	1.337	1.83E-2	7.29E-2	1.168
256	1.568	1.342	1.00E-2	4.41E-2	1.168

Table 4
Flow rates $Q^{(n)}$, $Q^{(d)}$ at $P_1/P_2 = 8$ and various values of σ versus $\delta_2^{(n)}$.

$\delta_2^{(n)}$	$Q^{(n)}$			$Q^{(d)}$		
	$\sigma = 1$	0.8	0.6	1	0.8	0.6
0.02	1.039	1.369	1.907	0.984	1.299	1.811
0.05	1.052	1.361	1.861	0.946	1.231	1.699
0.07	1.072	1.376	1.868	0.946	1.225	1.683
0.10	1.105	1.408	1.896	0.955	1.229	1.681
0.20	1.222	1.530	2.024	1.028	1.301	1.753
0.50	1.560	1.893	2.424	1.311	1.598	2.068
0.70	1.778	2.124	2.676	1.512	1.806	2.286
1	2.099	2.461	3.038	1.815	2.118	2.610
2	3.150	3.548	4.180	2.841	3.159	3.673
5	6.273	6.713	7.414	5.949	6.280	6.816

Table 5
Diodicity D at $P_1/P_2 = 8$ and various values of σ versus $\delta_2^{(n)}$.

$\delta_2^{(n)}$	D		
	$\sigma = 1$	0.8	0.6
0.02	1.055	1.054	1.053
0.05	1.112	1.105	1.095
0.07	1.133	1.124	1.110
0.10	1.158	1.146	1.128
0.20	1.189	1.176	1.155
0.50	1.190	1.184	1.172
0.70	1.176	1.176	1.170
1	1.157	1.162	1.164
2	1.109	1.123	1.138
5	1.054	1.069	1.088
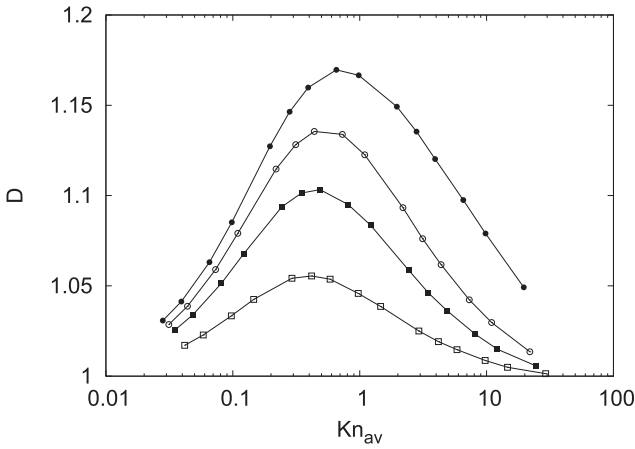
Fig. 1. Diodicity as a function of the average Knudsen number at $P_1/P_2 = 8$ versus H_l/H_s. Empty and filled squares and empty and filled circles stand for $H_l/H_s = [2, 4, 8, 128]$, respectively.

the whole nozzle flow configuration. It is well known that the dimensional mass flow rate monotonically decreases with increasing Knudsen number at constant pressure ratio since the gas becomes more rarefied if the Knudsen number is increased. If the gas is more rarefied, its density is smaller and the dimensional mass flow rate is also smaller. Since in the nozzle direction the mean Knudsen number is smaller than in the diffusor case, the mass flow rate is larger in the nozzle direction. As it was said at the end of section 2.2, the didodicity tends to zero in the hydrodynamic and free molecular limits. Hence, at intermediate rarefaction, there should be a maximum of the diodicity, which is found in the numerical simulation. These arguments explain well why the given behavior of the diodicity is obtained.

Fig. 2 shows the distributions of the pressure and the rarefaction parameter for the test channel with data $H_l/H_s = 120$, $W/H_s = 500$ and $\sigma = 1$ at various values of $\delta_2^{(n)}$ but fixed pressure ratio $P_1/P_2 = 8$. As it can be seen the pressure profile has a quite different character than what is observed for uniform channels, i.e. with constant cross sections. In the nozzle case, the pressure has a sharp variation at the end of the channel, where the cross section is relatively small. This phenomenon is caused by the smallness of the cross section. Since the mass flow rate is constant at each cross section, a larger pressure variation is necessary, where the cross section is small. This explains the stronger variation of the pressure as approaching the outlet of the channel where H_s is present. The opposite situation, when the pressure exhibits a strong variation near the beginning of the channel, is shown for the diffusor case. The rarefaction parameter for the nozzle case decreases along the flow direction since both pressure and L_c decrease in this direction. However, for the diffusor case, the rarefaction parameter increases along the axis. In this situation, the characteristic length L_c increases stronger along the channel than the pressure decreases.

Fig. 3 presents the profiles of the pressure and the rarefaction parameter for test channels with fixed width $W/H_s = 500$ but with various aspect ratios H_l/H_s at $\delta_2^{(n)} = 0.3$, $P_1/P_2 = 8$ and $\sigma = 1$. As it can be seen the pressure profile is quite sensitive to the ratio of the large and small heights. If H_l/H_s is small, e.g. $H_l/H_s = 2$, the pressure profile is similar to the one expected for a uniform channel with constant height. In this situation, the difference between the profiles in the nozzle and diffusor directions is small. If H_l/H_s is increased, the pressure profile tends to be more sharp near the small height. The figure shows that the axial distribution of the rarefaction parameter is also sensitive to the ratio of H_l/H_s. For small ratios, e.g. $H_l/H_s = 2$, the rarefaction parameter decreases along the axis of the channel, which is the typical behavior for uniform channels. In the opposite situation, if H_l/H_s is larger, the rarefaction parameter increases along the axis in the diffusor case. This behavior is caused by the increasing height along the flow direction.

3.2. Numerical and experimental flow rates

The experimentally measured mass flow rates are compared to the corresponding results of the numerical calculation. The experimental data is taken from Ref. [24]. For the details of the experimental measurement, the reader may consult that work. The temperature is $T \sim 21°C$. The molar masses of these gases are $m_{CO_2} = 44.01$ g/mol, $m_{N_2} = 28.01$ g/mol and $m_{Ar} = 39.95$ g/mol.

The viscosity of the gases is deduced on the basis of Refs. [29,30] at the proper temperature. In both nozzle and diffusor directions, the downstream pressure is in the range of $P_2 = [3.01 - 6.57]$ kPa, while the inlet pressure spans the range of $P_1 = [23.02 - 73.22]$ kPa. The corresponding inlet and outlet Knudsen numbers are in the range of $[2.61 \times 10^{-4} - 1.15 \times 10^{-3}]$, $[7.57 \times 10^{-1}, 2.26]$ for the nozzle and $[6.89 \times 10^{-2} - 3.01 \times 10^{-1}]$, $[2.92 \times 10^{-3} - 8.66 \times 10^{-3}]$ for the diffusor direction. The variation of the Knudsen number is quite large for the nozzle case, but it is just moderate for the diffusor one. For all calculations complete accommodation is used $\sigma = 1$.

Tables 6 and 7 show the comparison between numerical and experimental results for the nozzle and diffusor directions. Two types of numerical result are shown. Computational data denoted by subscripts $c1$ and $c2$ are results calculated by using the long channel assumption and that calculation with an end-correction, respectively. The end-correction is calculated on the basis of Refs. [31,32] by adding a suitable correction ΔL to the channel

Fig. 2. Distributions of the pressure (a) and the rarefaction parameter (b) along the axis of the test channel for nozzle and diffusor directions at $P_1/P_2 = 8$. Squares, circles and triangles denote the profiles for $\delta_2^{(n)} = [0.06, 0.2, 0.3]$. Empty and filled symbols represent the results for the nozzle and diffusor directions, and the left and right vertical axes for the rarefaction parameter on subfigure (b) corresponds to the nozzle and diffusor cases, respectively. The pressure is normalized by $P_r = P_2$ at $\delta_2^{(n)} = 0.06$.
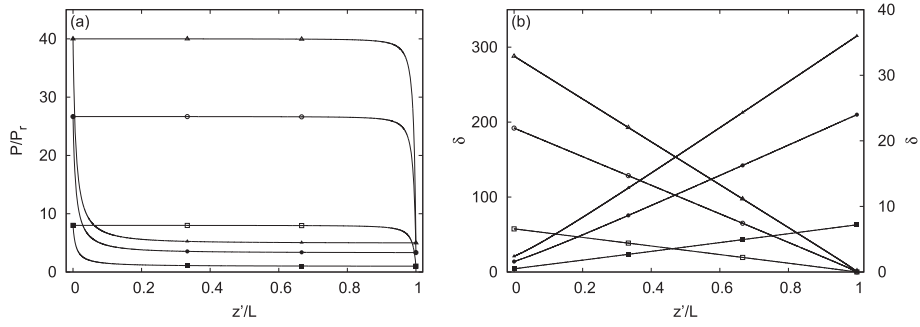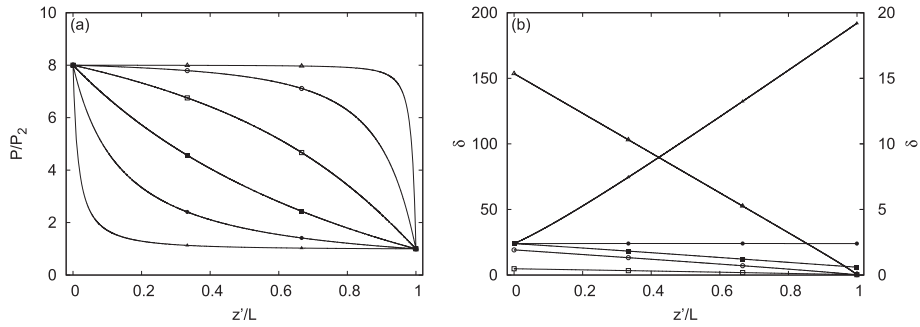

Fig. 3. Distributions of the pressure (a) and the rarefaction parameter (b) along the axis of test channels for nozzle and diffusor directions at $\delta_2^{(n)} = 0.3$ and $P_1/P_2 = 8$ as functions of the large to small height ratio. Squares, circles, triangles denote the results for $H_l/H_s = [2, 8, 64]$. Empty and filled symbols stand for the nozzle and diffusor directions, and the left and right vertical axes for the rarefaction parameter on subfigure (b) corresponds to the nozzle and diffusor cases, respectively.

Table 6
Numerical $\dot{M}_{c1}, \dot{M}_{c2}$ and experimental $\dot{M}_e$[24] flow rates for nozzle direction for CO_2, N_2 and Ar gases. The last two columns show the absolute relative difference between the experimental and numerical flow rates $\Delta_1 = \left| \dot{M}_e/\dot{M}_{c1} - 1 \right|$ and $\Delta_2 = \left| \dot{M}_e/\dot{M}_{c2} - 1 \right|$ for the normal and end-corrected calculation, respectively.

	P_1(Pa)	P_2(Pa)	$\dot{M}_{c1}$(µg/s)	$\dot{M}_{c2}$(µg/s)	$\dot{M}_e$(µg/s)	Δ_1(%)	Δ_2(%)
CO_2	23015	3014	3.190	3.150	2.588	18.9	17.9
	28368	3375	4.301	4.247	3.656	15.0	13.9
	33723	3747	5.534	5.466	4.847	12.4	11.3
	39084	4123	6.891	6.806	6.139	10.9	9.8
	44462	4508	8.375	8.271	7.542	9.9	8.8
	55191	5243	11.709	11.564	10.662	8.9	7.8
	66207	6023	15.638	15.444	14.354	8.2	7.1
N_2	25498	3317	2.572	2.540	1.848	28.1	27.2
	31437	3717	3.421	3.378	2.611	23.7	22.7
	37029	4085	4.295	4.242	3.462	19.4	18.4
	42916	4491	5.294	5.228	4.384	17.2	16.1
	48806	4911	6.367	6.288	5.387	15.4	14.3
	60665	5726	8.780	8.671	7.615	13.3	12.2
	72272	6573	11.566	11.423	10.252	11.4	10.2
Ar	23916	3217	2.773	2.738	1.998	27.9	27.0
	29486	3548	3.681	3.635	2.822	23.3	22.4
	34839	3912	4.622	4.565	3.759	18.6	17.6
	40365	4290	5.673	5.603	4.762	16.1	15.0
	46037	4699	6.830	6.745	5.832	14.6	13.5
	57158	5466	9.348	9.232	8.245	11.8	10.7
	68618	6295	12.265	12.112	11.092	9.6	8.4

Table 7
Numerical $\dot{M}_{c1}, \dot{M}_{c2}$ and experimental $\dot{M}_e$[24] flow rates for diffusor direction for CO_2, N_2 and Ar gases. The last two columns show the absolute relative difference between the experimental and numerical flow rates $\Delta_1 = \left| \dot{M}_e/\dot{M}_{c1} - 1 \right|$ and $\Delta_2 = \left| \dot{M}_e/\dot{M}_{c2} - 1 \right|$ for the normal and end-corrected calculation, respectively.

	P_1(Pa)	P_2(Pa)	$\dot{M}_{c1}$(µg/s)	$\dot{M}_{c2}$(µg/s)	$\dot{M}_e$(µg/s)	Δ_1(%)	Δ_2(%)
CO_2	23039	3027	2.753	2.719	2.411	12.4	11.3
	28368	3363	3.712	3.666	3.404	8.3	7.1
	33713	3708	4.787	4.728	4.513	5.7	4.6
	39059	4072	5.981	5.907	5.733	4.1	3.0
	44424	4446	7.298	7.208	7.067	3.2	2.0
	55131	5170	10.291	10.164	10.049	2.3	1.1
	66157	5940	13.874	13.703	13.653	1.6	0.4
N_2	25515	3304	2.209	2.181	1.722	22.0	21.0
	31428	3681	2.928	2.891	2.431	16.9	15.9
	37334	4076	3.722	3.676	3.224	13.4	12.3
	43261	4472	4.594	4.538	4.095	10.9	9.8
	49180	4880	5.542	5.474	5.048	8.9	7.8
	61008	5674	7.671	7.576	7.178	6.4	5.3
	73222	6532	10.193	10.067	9.751	4.3	3.1
Ar	24156	3189	2.415	2.386	1.855	23.2	22.2
	29851	3505	3.202	3.162	2.619	18.2	17.2
	35094	3884	3.991	3.941	3.494	12.4	11.3
	40420	4284	4.857	4.797	4.440	8.6	7.4
	46063	4697	5.856	5.784	5.459	6.8	5.6
	57181	5464	8.051	7.952	7.762	3.6	2.4
	68652	6292	10.639	10.508	10.537	1.0	0.3

length L. ΔL is determined on the basis of Refs. [31,32]. Since there are no published results for a rectangular cross section, at the end of the duct with the large height, the end effect is approximated by using an equivalent tube with the same hydraulic diameter as the tapered duct has [32]; on the other hand, the end-effect of flows between two parallel plates is used at the small cross section [31].

For the experimental comparison, the rarefaction parameter at the large cross section is so large in all cases that the end-correction in the hydrodynamic limit is used [32]. For the small cross section, the end-correction at the given rarefaction parameter is applied [31]. Interpolated values are used when the exact correction is not available in Ref. [31].

The columns of Table 6 from left to right present the inlet and outlet pressures, the two types of calculated and experimental flow rates ($\dot{M}_{c1}$, $\dot{M}_{c2}$ and $\dot{M}_e$) and the relative differences between $\dot{M}_{c1}$, $\dot{M}_{c2}$ and $\dot{M}_e$ defined as $\Delta_1 = \left| \dot{M}_e / \dot{M}_{c1} - 1 \right|$, $\Delta_2 = \left| \dot{M}_e / \dot{M}_{c1} - 2 \right|$. Table 7 presents the same quantities for the diffusor direction. It can be seen that there is a relatively good agreement between the numerical and experimental flow rates. The average of the relative difference Δ_1 is 12.0%, 18.4%, 17.4% for the nozzle and 5.4%, 11.8%, 10.5% for the diffusor case for CO_2, N_2 and Ar gases, respectively. The same values for Δ_2 are 10.9%, 17.3%, 16.4% and 4.2%, 10.7%, 9.4%, respectively. The average difference is larger for the nozzle direction than the diffusor one. Both numerical and experimental flow rates confirm the diode effect, i.e. the flow rate is larger for the nozzle case than the corresponding diffusor one. The difference between the two types of approach depends on the quality of the gas. As it can be seen the end-corrected numerical results better predict the experimental flow rates than the non-corrected ones.

The agreement between the numerical and experimental flow rates is better than in Ref. [24] in all cases. For the long channel assumption, this better agreement can be reasoned by the more accurate viscosity function. In Ref. [24], the viscosity was defined by the variable hard sphere (VHS) model, while in the present case that is obtained from experimental data [29,30], which is considered as more accurate than the VHS model. For the end-corrected results, the improvement is caused by the end-correction. The end-effect could be totally captured by doing alternative simulations with the inclusion of the inlet and outlet reservoirs. However, this would require a completely different simulation method, which is beyond the scope of the present paper. For both corrected and non-corrected numerical results, the sources of the aforementioned differences between the numerical and experimental results can be: 1) the mass flow controller might slightly underestimate the flow rate for its smaller values, 2) the maximum of the Mach number is larger in the nozzle direction than the diffusor one [25,26]. The effect of the higher Mach number in the nozzle direction is not captured by the linearized theory.

The present calculation is based on the linearized BGK model. Some part of the discrepancy between the experimental and numerical results can also be devoted to the modeling error introduced by the BGK equation. However, it is known that the BGK model provides a relatively good approximation of pressure driven flows of simple polyatomic (like N_2 and CO_2) and noble (like Ar) gases. Poiseuille flow through long circular tubes and between parallel plates has been calculated for polyatomic gases by using the Hansen and Morse polyatomic gas model in the linearized Wang, Chang and Uhlenbeck equation in a wide range of the gas rarefaction [33–36]. For flow between two plates, the absolute relative difference between the dimensionless flow rates of the polyatomic model and the BGK equation does not exceed 0.6% and 1.5% for all investigated parameters of nitrogen and for carbon-dioxide gases, respectively. For circular tube, the same quantity is not larger than 0.7% and 0.1% for the studied cases of nitrogen and carbon-dioxide, respectively.[1] Another approach, the Rykov polyatomic model, has been solved for Poiseuille flows with parameters for nitrogen gas in long circular tubes and between two parallel plates [37]. For circular tube, the absolute relative difference between the flow rates of the Rykov model and the BGK equation [34] is not larger than 1%. For flows between two parallel plates, the same quantity between the results of the Rykov model and the present BGK solver does not exceed 0.7%. For the present

experiment with Ar, the rarefaction parameter is $\delta \geq 0.4$. In this range, the absolute relative differences between the flow rates calculated by using the linearized Boltzmann equation with the Lennard-Jones potential and the BGK model is not larger than 4.5% for flows between two parallel plates [38]. By using these results, we estimate that the modeling error of the linearized BGK equation for Poiseuille flows of the present gases for the flow rate is not larger than 4.5%.

Comparison between experimental flow rates and numerical results on the basis of the linearized BGK equation can be found in Refs. [9,22] for N_2 and Ar gases, respectively. In Ref. [9], the error between the experimental and numerical flow rates is found to be less than 10% with an average value of 5%. In Ref. [22], the difference between the experimental and numerical results is within the experimental error ±4% for Ar gas. The experimental errors are always subjects of various factors, like uncertainty of geometrical data, temperature and pressure measurements. By using the recent experimental techniques, it is not possible to better predict the modeling error of the BGK and other related models for pressure driven flows of mono-atomic or polyatomic gases than $4\% - 5\%$ because the modeling error is smaller or in the range of the experimental uncertainties.

Table 8 presents the computational diodicities D_{c1} for the normal calculation and the experimental one D_e for the three gases. The relative differences between these quantities $\Delta_{d1} = |D_e / D_{c1} - 1|$ is also shown. It can be seen that there is good agreement between the diodicities also. The difference is in the same range as in Ref. [24]. The end-corrected diodicities D_{c2} are also calculated, but those are identical with D_{c1} for four-figure accuracy except ±1 difference in the last shown digit in one case. Hence, D_{c2} and its absolute relative difference to D_e are not shown in the table. The calculated diodicity is always larger than the corresponding experimental value. This indicates that there is a systematic over-prediction of the flow rate in the nozzle direction than the diffusor one in the numerical simulation. This over-prediction can be caused by the larger Mach number in the nozzle direction [25,26]. However, further analysis of this effect is out of the scope of the paper. The didocity is a derived quantity, and the primary one is the flow rate. In terms of this latter, the present study provides a better agreement with the experimental data than Ref. [24].

---

[1] For the BGK results for circular tube, it seems that there is a misprint in Table 4 in Ref. [34] at inverse Knudsen number $R = 0.75$; hence, that case is not considered.

Table 8
Computational D_{c1} and experimental D_e[24] diodicities and their absolute relative difference $\Delta_{d1} = |D_e / D_{c1} - 1|$ for CO_2, N_2 and Ar gases for pressures given in Tables 6 and 7

	D_{c1}	D_e	Δ_{d1} (%)
CO_2	1.161	1.075	7.4
	1.159	1.074	7.3
	1.156	1.074	7.1
	1.151	1.070	7.0
	1.146	1.066	7.0
	1.136	1.059	6.7
	1.126	1.050	6.7
N_2	1.166	1.075	7.8
	1.168	1.074	8.1
	1.173	1.092	6.9
	1.171	1.088	7.1
	1.167	1.084	7.1
	1.158	1.073	7.3
	1.149	1.065	7.3
Ar	1.172	1.100	6.1
	1.179	1.105	6.3
	1.176	1.092	7.1
	1.171	1.075	8.2
	1.168	1.070	8.4
	1.162	1.063	8.5
	1.154	1.054	8.7

4. Conclusions

In this paper, pressure driven rarefied single gas flows through long tapered rectangular channels have been analyzed computationally. The mass flow rates are compared to the corresponding experimental data [24]. The numerical approach refers to the solution of the linearized BGK kinetic equation. The mass flow rate and the distributions of the pressure and the rarefaction parameter have been deduced for flows through test channels in the whole range of the gaseous rarefaction and at various other flow parameters. The diodicity, the scaled ratio of the flow rates in the nozzle and diffusor directions, has been determined. It has a maximum as a function of the gaseous rarefaction. The results indicate that for achieving a maximal diode efficiency, there is an optimal rarefaction degree in the transition region. The diodicity in both hydrodynamic and free molecular limits is unity. The effect of the accommodation coefficient is studied on the flow rate and the diodicity. The pressure profile exhibits a rapid change near the end of the channel at the small cross section. For the nozzle direction, the rarefaction parameter always decreases along the axis of the channel, while, in the opposite direction, it decreases only if the ratio of the small and large cross sections is sufficiently small, and it increases otherwise. The mass flow rate of CO_2, N_2, Ar gases through a mini/microchannel has been compared to the results of the kinetic calculation at moderate rarefactions. End-corrections are applied to the numerical simulation in order to better predict the flow rate. A relatively good agreement has been found between the experimental and numerical results. The end-correction improves this agreement. The present results can provide more insight into flows through channels with varying cross sections and might be useful in the optimal design of pumping systems which are based on the diode effect.

References

[1] S.G. Kandlikar, S. Garimella, et al., Heat Transfer and Fluid Flow in Mini-channels and Microchannels, Elsevier, Oxford, 2006.
[2] K. Jousten (Ed.), Handbook of Vacuum Technology, Wiley-VCN, 2008.
[3] F. Sharipov, J. Vac. Sci. Technol. A 17 (1999) 3062–3066.
[4] F. Sharipov, V. Seleznev, J. Vac. Sci. Technol. A 12 (1994) 2933–2935.
[5] L. Szalmas, Comput. Phys. Commun. 184 (2013) 1432–1438.
[6] I. Graur, F. Sharipov, Eur. J. Mech. B/Fluids 27 (2007) 335–345.
[7] S. Naris, D. Valougeorgis, Eur. J. Mech. B/Fluids 27 (2008) 810–822.
[8] L. Szalmas, D. Valougeorgis, J. Comput. Phys. 229 (2010) 4315–4326.
[9] S. Varoutis, S. Naris, V. Hauer, C. Day, D. Valougeorgis, J. Vac. Sci. Technol. A 27 (2009) 89–100.
[10] L. Szalmas, Vacuum 109 (2014) 302–307.
[11] S. Naris, D. Valougeorgis, D. Kalempa, F. Sharipov, Superlattices Microstruct. 35 (2004) 629–643.
[12] L. Szalmas, D. Valougeorgis, Microfluid. Nanofluid. 9 (2010) 471–487.
[13] S. Varoutis, S. Naris, V. Hauer, C. Day, D. Valougeorgis, J. Vac. Sci. Technol. A 27 (2009) 89–100.
[14] L. Szalmas, Comput. Phys. Commun. 184 (2013) 2430–2437.
[15] F. Sharipov, G. Bertoldo, J. Vac. Sci. Technol. A 23 (2005) 531–533.
[16] I. Graur, M.T. Ho, Vacuum 101 (2014) 328–332.
[17] E.B. Arkilic, M.A. Schmidt, K.S. Breuer, J. Microelectromech. Syst. 6 (1997) 167–178.
[18] E.B. Arkilic, K.S. Breuer, M.A. Schmidt, J. Fluid Mech. 437 (2001) 29–43.
[19] Y. Zohar, S.Y.K. Lee, W.Y. Lee, L. Jiang, P. Tong, J. Fluid Mech. 472 (2002) 125–151.
[20] S. Colin, P. Lalonde, R. Caen, Heat. Transf. Eng. 25 (2004) 23–30.
[21] T.P. Ewart, P. Perrier, I.A. Graur, J.G. Meolans, Exp. Fluids 41 (2006) 487–498.
[22] J. Pitakarnnop, S. Varoutis, D. Valougeorgis, S. Geoffroy, L. Baldas, S. Colin, Microfluid. Nanofluid. 8 (2010) 57–72.
[23] T. Veltzke, M. Baune, J. Thoming, Phys. Fluids 24 (2012), 082004.
[24] I. Graur, T. Veltzke, J.G. Meolans, M.T. Ho, J. Thoming, Microfluid. Nanofluid. 18 (2015) 391–402.
[25] V. Varade, A. Agrawal, A.M. Pradeep, J. Mircomech. Microeng. 25 (2015), 025015.
[26] V. Varadea, V.S. Duryodhanb, A. Agrawal, A.M. Pradeepc, A. Ebrahimid, E. Roohid, Comput. Fluids 111 (2015) 46–62.
[27] A. Olsson, G. Stemme, E. Stemme, Sens. Actuat. A-Phys. 47 (1995) 549–556.
[28] T. Gerlach, M. Schuenemann, H. Wurmus, J. Micromech. Microeng. 5 (1995) 199–201.
[29] A. Boushehri, J. Bzowski, J. Kestin, E.A. Mason, J. Phys. Chem. Ref. Data 16 (1987) 445–466.
[30] J. Kestin, K. Knierim, E.A. Mason, B. Najafi, S.T. Ro, M. Waldman, J. Phys. Chem. Ref. Data 13 (1984) 229–303.
[31] S. Pantazis, D. Valougeorgis, F. Sharipov, Vacuum 97 (2013) 26–29.
[32] S. Pantazis, D. Valougeorgis, F. Sharipov, Vacuum 101 (2014) 306–312.
[33] S.K. Loyalka, T.S. Storvick, J. Chem. Phys. 71 (1979) 339–350.
[34] S.K. Loyalka, T.S. Storvick, S.S. Loa, J. Chem. Phys. 76 (1982) 4157–4170.
[35] S.S. Lo, S.K. Loyalka, T.S. Storvick, J. Chem. Phys. 81 (1984) 2439–2449.
[36] S.K. Loyalka, S.S. Lo, J. Vac. Sci. Technol. A 7 (1989) 2766–2773.
[37] V.A. Titarev, E.M. Shakov, Fluid Dyn. 47 (2012) 661–672.
[38] F. Sharipov, G. Bertoldo, Phys. Fluids 21 (2009), 067101/1–8.